

INTERMEDIATE-LINE EMISSION IN AGNS: THE EFFECT OF PRESCRIPTION OF THE GAS DENSITY

T. P. ADHIKARI¹, K. HRYNIEWICZ¹, A. RÓŻAŃSKA¹, B. CZERNY² AND G. J. FERLAND^{3,1}

¹Nicolaus Copernicus Astronomical Center, Polish Academy of Sciences, Bartycka 18, 00-716, Warsaw

²Center for Theoretical Physics, Polish Academy of Sciences, Aleja Lotnikow 32/46, Warsaw, Poland

³Department of Physics and Astronomy, The University of Kentucky, Lexington, KY 40506, USA

ABSTRACT

The requirement of intermediate line component in the recently observed spectra of several AGNs points to possibility of the existence of a physically separate region between broad line region (BLR) and narrow line region (NLR). In this paper we explore the emission from intermediate line region (ILR) by using the photoionization simulations of the gas clouds distributed radially from the AGN center. The gas clouds span distances typical for BLR, ILR and NLR, and the appearance of dust at the sublimation radius is fully taken into account in our model. Single cloud structure is calculated under the assumption of the constant pressure. We show that the slope of the power law cloud density radial profile does not affect the existence of ILR in major types of AGN. We found that the low ionization iron line, Fe II, appears to be highly sensitive for the presence of dust and therefore becomes potential tracer of dust content in line emitting regions. We show that the use of disk-like cloud density profile computed at the upper part of the accretion disc atmosphere reproduces the observed properties of the line emissivities. In particular, the distance of H β line inferred from our model agrees with that obtained from the reverberation mapping studies in Sy1 galaxy NGC 5548.

Keywords: galaxies: active - methods: numerical - radiative transfer - quasars: emission lines

1. INTRODUCTION

Over the past several decades, the properties and origin of broad line region (BLR) as well as narrow line region (NLR) in active galactic nuclei (AGN) are extensively discussed in the literatures (Davidson 1972; Krolik, McKee & Tarter 1981; Netzer 1990; Dopita et al. 2002; Baskin, Laor & Stern 2014; Czerny & Hryniewicz 2011; Czerny et al. 2015, 2017, and references therein). There is a general consensus that both regions are physically separate and spatially located at different distances from the central supermassive black hole (SMBH) of AGN. The above conclusion naturally came from the lack of any significant emission from lines with full width at half maximum (FWHM) between ~ 2000 km s⁻¹, typical for BLR, and ~ 500 km s⁻¹, typical for NLR (Boroson & Green 1992).

Theoretically, the lack of such emission from gas between BLR and NLR was successfully explained by Netzer & Laor (1993, hereafter NL93). The authors calculated the line emission from radially distributed clouds above an accretion disk, using photoionization computations. Each cloud was a constant density slab illuminated by the same mean quasar continuum shape. The

lack of line emission was successfully achieved with the introduction of dust. Practically it means, that the dust was taken into account in photoionization calculations for clouds located further away from SMBH at the certain radius named sublimation radius. Closer to the nucleus the radiation field is so strong that the dust grains cannot survive. The presence of dust for a given gas conditions successfully suppresses line emission, and the gap between BLR and NLR is naturally formed. However, new observations with the largest instruments give us a new look at those objects.

There is a growing number of AGN which exhibit the emission lines with intermediate FWHM ~ 700 – 1200 km s⁻¹ in their spectra suggesting the existence of intermediate line region (ILR) in those sources. Brotherton et al. (1994) have defined ILR in 15 broad UV line QSO as the second component of BLR, located at most inner part of NLR.

Mason, Puchnarewicz & Jones (1996) found evidence for an ILR with velocity FWHM ~ 1000 km s⁻¹ which produces a significant amount of both permitted and forbidden line fluxes in ultra-soft X-ray source NLSy1 RE J1034+396. H α , H β , O [III] observed by ISIS spectrograph La Palma. Detailed spectral analysis of large number of SDSS sources have revealed the presence of intermediate component of line emission with velocity

width in between that of broad and narrow component (Hu et al. 2008a,b). *SDSS* sources show ILR in H α and H β lines (Zhu, Zhang & Tang 2009), mostly for NLSy1 galaxies.

For the Sy1 NGC 4151, Crenshaw & Kraemer (2007) identified an intermediate line emission component with width FWHM = 1170 km s⁻¹, most probably originating between the BLR and NLR. For Sy1 NGC 5548, ILR was found to be located at ~ 1 pc, with smaller velocity FWHM = 680 km s⁻¹ Crenshaw et al. (2009).

Moreover, the presence of ILR in 33 galaxies with low ionization nuclear emission-line regions (so called LINERs) was reported by Balmaverde et al. (2016) using HST/STIS (Hubble Space Telescope/Space Telescope Imaging Spectrograph). Since typical obscuration torus is not present in LINERs, the authors suggest that the ILR takes the form of an ionized, optically thin torus. They also suggest that this tenuous structure is present only in LINERs because of the general paucity of gas and dust in their nuclear regions. This also causes their low rate of accretion and low bolometric luminosity.

Recently, Adhikari et al. (2016, hereafter AD16) studied the ILR by using the photoionization simulations of an ionized gas with dust in AGN. Within the framework of NL93 formalism, the authors found that in order to expect ILR emission the density of gas should be high, of the order of $\sim 10^{11.5}$ cm⁻³ at the sublimation radius, which means that for each cloud located at the certain distance the density in AD16 paper was two orders of magnitude higher than in NL93. For such dense matter the gas opacities always dominates over the dust opacities in a region of the line formation, and the dust cannot suppress the line emission as it was present in NL93 paper. Therefore, the usual gap between BLR and NLR can not be created, and ILR can be present. The above result was achieved for three different spectral shapes of illuminated continuum typical for Sy1.5, Sy1 and NLSy1 AGN. In addition, AD16 argued that the LINERs should also exhibit the ILR emission, due to the low value of luminosity and therefore the ionization parameter in those sources.

The aim of the paper is to investigate in details the physics of ILR. We extend our previous studies (AD16) by: (i) performing computations for constant pressure (CP) instead of constant density (CD) cloud model, (ii) searching the influence of power-law density slope on the total line emission, (iii) including additional emission lines as Fe II and C IV, (iv) considering the disk-like cloud density profile from accretion disk atmosphere, (v) using self-consistent source luminosities and therefore the position of the sublimation radius.

We perform the photoionization simulations by publicly available numerical code CLOUDY version C17.00 (Ferland et al. 2017), assuming that each cloud is under

constant pressure (Baskin, Laor & Stern 2014). In the first step, we consider the model of continuous cloud distribution above an accretion disk, following approach of AD16. Nevertheless, we vary the power law index which relates to the surface cloud density distribution within the distance from SMBH. We show, that the existence of the ILR is not sensitive to the slope of density power-law profile considered by us with the assumption of CP cloud. The same result was obtained by Adhikari et al. (2017), in case of CD clouds.

In the second step, for each of four sources, we compute source luminosities and we use those values to derive the position of sublimation radius according to formula given by Nenkova et al. (2008). This allows us implement dust correctly in our photoionization calculations. To achieve the physically consistent density profile, we assume that clouds are created from upper parts of an accretion disk. By adopting black hole masses and accretion rates of four considered sources, given in the literatures, we simulate the vertical accretion disk structure assuming standard Shakura & Sunyaev (1973) disk and transfer of radiation by diffusion approximation (Róžańska et al. 1999). Furthermore, we employ the radial density profile obtained by solving the vertical accretion disk structure of geometrically thin disk at optical thickness $\tau=2/3$ as described in section 4. This can only be done by straight comparison of cloud density with density of an upper disk atmosphere at a given radius. This idea is very close to the development done by Baskin & Laor (2018) who associates BLR directly with accretion disk atmosphere.

For disk-like cloud density profile, we obtained the prominent ILR in all four sources considered. However, the sublimation radius for LINER NGC 1097 is smaller by ~ 2 orders of magnitude than rest of the sources because of its low luminosity. The density drop in disk-like density profile causes mild enhancement of low ionization lines (LIL), while high ionization lines (HIL) are suppressed at the density drop location. This result is in agreement with two-component BLR model presented by Collin-Souffrin et al. (1988). The distance inferred from the time delay of H β in NGC 5548 taken from observations agrees with the distance at which the H β line peaks in our simulated line emissivity profile.

The structure of the paper is organized as follows. In Sec. 2, we describe the numerical model parameters taken for the photoionization computations. Whole Sec. 3 is devoted to the effect of slope of the power law density profile on the computed line emission. In addition, the comparison of CP with CD model is explicitly shown in subsection 3.1, while dust sensitive line Fe II is discussed in 3.4. Sec. 4 contains the results we obtained for the disk-like density prescription we adopted. Finally the discussion of line emission and conclusions

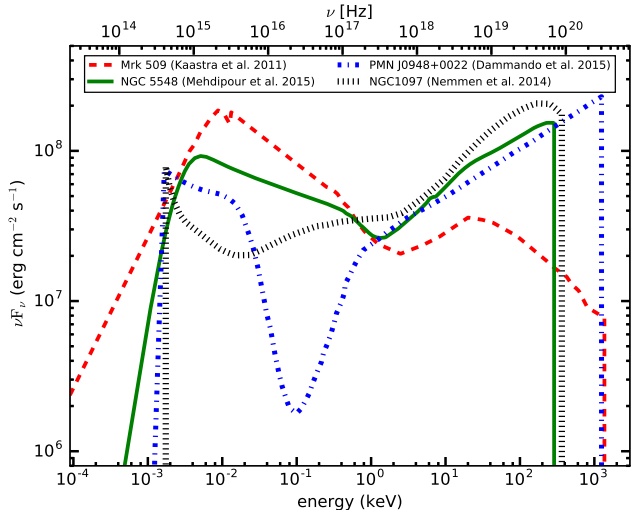


Figure 1. Shapes of the broad band spectra used in our photoionization calculations. In order to see the dependence on spectral shape all SEDs are normalized to the $L_{\text{bol}} = 10^{45} \text{ erg s}^{-1}$. See Table 1 for the exact values of luminosities.

are presented in Sec. 5 and Sec. 6 respectively.

2. PHOTOIONISATION SIMULATIONS OF ILR

In order to achieve the established properties of ionized gas located at different distances from SMBH, which can be responsible for the observed broad to narrow line emission, we consider a distribution of clouds above an accretion disk, defined at each radial distance, r , by the gas density n_{H} at a cloud surface, total column density N_{H} , and the chemical abundances. Photoionization processes are simulated with numerical code CLOUDY version C17 (Ferland et al. 2017).

We used the CLOUDY default solar abundances derived by Grevesse & Sauval (1998), for the gas clouds being at the distance $r \leq R_{\text{d}}$, where we expect that BLR is located. For the clouds at $r > R_{\text{d}}$, where NLR suppose to occur, the interstellar medium composition (ISM) with dust grains is used¹. Depending on the radial density profile, we consider various values of sublimation radius R_{d} , expressed in two sections below: Section 3 and 4.

In all radially distributed cloud models, we adopt the profile for the column density after NL93 and AD16:

$$N_{\text{H}}(r) = 10^{23.4} (r/R_{\text{d}})^{-1} \quad (1)$$

The normalization value of column density, $N_{\text{H}} = 10^{23.4} \text{ cm}^{-2}$, again is taken from NL93 and AD16 due to general agreement of the observed BLR column density.

For a given radial distance, the cloud pressure is kept constant (Baskin, Laor & Stern 2014). Practically it means that the gas pressure increases with

cloud optical depth as radiation pressure decreases exponentially with gas optical depth. This option of photoionization computations was incorporated in CLOUDY as radiation pressure confinement (RPC), and used by Baskin, Laor & Stern (2014) for the purpose of BLR. The concept of RPC does not differ from the total CP models used by Rózańska et al. (2006); Rózańska, Kowalska & Gonçalves (2008); Adhikari et al. (2015) in case of the warm absorbers in AGN. The only difference is in numerical treatment of the radiation pressure, which in case of second group of authors is self consistently computed from the true intensity radiation field (see Dumont, Abrassart & Collin 2000, for description of TITAN code). Nevertheless, for both approaches, the input parameter as hydrogen number density of individual cloud, n_{H} , is given only at the cloud surface. This is because the radiation pressure compresses the cloud and the density gradient across the photoionized gas occurs naturally, which is self consistently computed by CLOUDY code. The exact comparison of CP and CD models for the purpose of ILR is given in Sec. 3.1.

For the radial distribution of clouds, the density number assumed at each cloud surface changes with distance from SMBH according to a given radial profile of the density at cloud surface $n_{\text{H}}(r)$. The exact radial density profiles used in our computations are given in Sec. 3 and 4 below.

The ionized clouds are distributed from $r = 10^{-2}$ up to $r = 10^3 \text{ pc}$. For the given cloud location and for the given density at the cloud surface, the ionization parameter U is computed by the CLOUDY code using the well known expression (Osterbrock & Ferland 2006):

$$U = \frac{Q_{\text{H}}}{4\pi r^2 n_{\text{H}} c} \quad (2)$$

where Q_{H} is the number of hydrogen ionising photons in the incident radiation field and c is the velocity of light.

In all our models of radially distributed clouds, we assume that each cloud is illuminated by the same shape of SED. We consider four shapes of SED adopted from recent multi-wavelength observations of: Sy1.5 - Mrk 509 (Kaastra et al. 2011), Sy1 - NGC 5548 (Mehdipour et al. 2015), NLSy1 galaxy PMN J0948+0022 (D’Ammando et al. 2015), and LINER - NGC 1097 (Nemmen, Storchi-Bergmann & Eracleous 2014) as displayed in Fig. 1. In order to see spectral shape of different type of AGN, we normalized all SEDs to $L_{\text{bol}} = 10^{45} \text{ erg s}^{-1}$ in this figure. This value is used in all calculations presented in Sec. 3, while in Sec. 4 luminosities are taken directly from integrations of observations.

All final conclusions of our paper are based on analysis the modelled line emissivity profiles given as an

¹ see Hazy1 CLOUDY documentation for the details

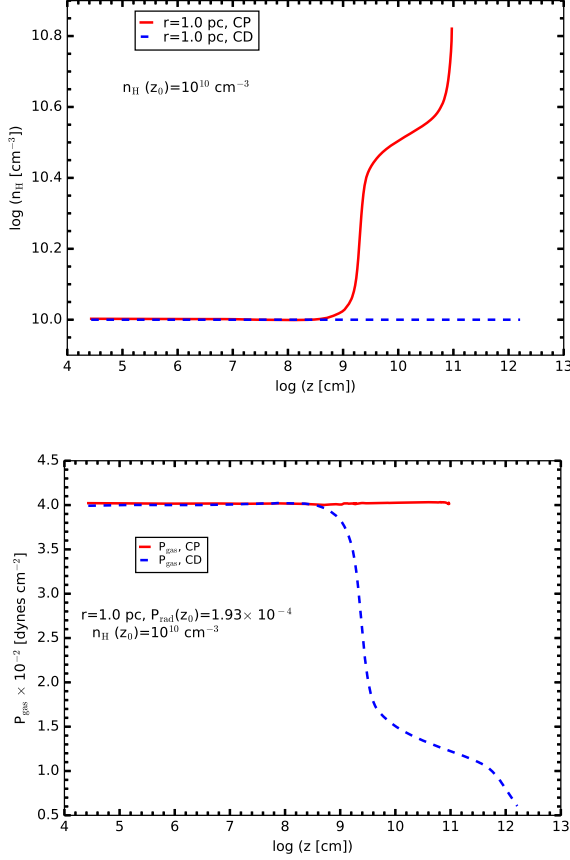


Figure 2. The comparison of constant density (CD) and constant pressure (CP) model for a single cloud with the density: $n_{\text{H}} = 10^{10} \text{ cm}^{-3}$ at the illuminated cloud surface. The Mrk 509 SED is used in both simulations. The density and gas pressure stratifications are shown in upper and lower panel, respectively.

output of photoionization calculation. In the case of each source we present radial emissivity profiles for the most observed line transitions in the AGN spectra: H β λ 4861.36 Å, He II λ 1640.00 Å, Mg II λ 2798.0 Å, C III] λ 1909.00 Å, [O III] λ 5006.84 Å, Fe II λ (4434-4684) Å, and C IV λ 1549.00 Å.

3. POWER LAW DENSITY PROFILE

In order to investigate the influence of the density profile on the emission line luminosity versus radius, in this section we assume that the density at the cloud surface decreases with distance from the SMBH as:

$$n_{\text{H}} = 10^{11.5} (r/R_{\text{d}})^{-\beta} \quad (3)$$

where β is the power law density slope. The value of the density at the cloud surface at the sublimation radius, R_{d} , (i.e. density normalization) is adopted after AD16. This is because, AD16 have shown that only for such high density value ILR can exist in the framework of this model. For all models computed in this section

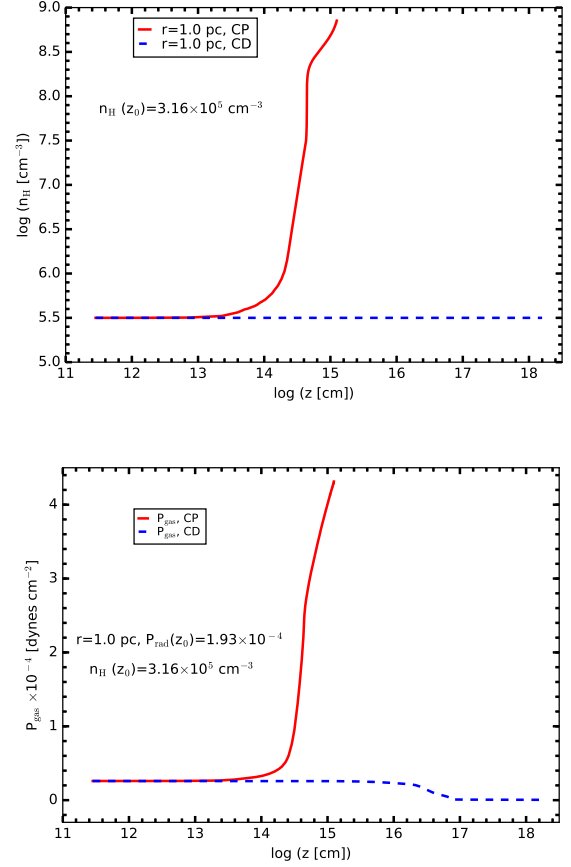


Figure 3. The same as in Fig. 2, but for low density cloud with: $n_{\text{H}} = 3.16 \times 10^5 \text{ cm}^{-3}$ at the illuminated cloud surface.

we adopt the same sublimation radius: $R_{\text{d}} = 0.1 \text{ pc}$, following NL93 and AD16.

For the density profile given by Eq. 3, the resulting ionization parameter U depends on the cloud location and on the amount of ionizing photons (Eq. 2). Assuming the same bolometric luminosity: $L_{\text{bol}} = 10^{45} \text{ erg s}^{-1}$, in case of four sources, we obtain following scaling laws of the ionization parameter with distance in pc:

$$U_{\text{Mrk509}} = 6.72 \times 10^{-6} (r/R_{\text{d}})^{\beta} r^{-2} \quad (4)$$

$$U_{\text{NGC5548}} = 3.11 \times 10^{-6} (r/R_{\text{d}})^{\beta} r^{-2} \quad (5)$$

$$U_{\text{NGC1097}} = 1.13 \times 10^{-6} (r/R_{\text{d}})^{\beta} r^{-2} \quad (6)$$

$$U_{\text{PMNJ0948}} = 1.08 \times 10^{-6} (r/R_{\text{d}})^{\beta} r^{-2} \quad (7)$$

For the purpose of this paper, we consider three values of $\beta = 0.5, 1.5, 2.5$, which are taken as arbitrary numbers to relate density as different powers of distance. We note that $\beta = 1.5$ converges to the profile used by NL93 and AD16.

3.1. CP versus CD for a single cloud

We consider a single cloud in the spherically symmetric gravitational field, located at radial distance r from the SMBH. We assume that locally the cloud thickness is negligible in comparison to the distance which is equivalent to locally plane parallel approximation of the cloud geometry. The cloud is illuminated by radiation flux F_0 at the illuminated face z_0 . The condition of hydrostatic equilibrium, for black hole mass M_{BH} , with optical depth as a variable $d\tau = \kappa \rho dz$, is:

$$\frac{dP_{\text{gas}}}{d\tau} = -\frac{1}{\kappa} \left(\frac{GM_{\text{BH}}}{r^2} - \Omega^2 r \right) - \frac{dP_{\text{rad}}}{d\tau} \quad (8)$$

where as usual ρ is volume density, κ - mean opacity coefficient, G - gravitational constant, P_{gas} and P_{rad} - gas and radiation pressure, and Ω is the gas angular velocity. Expressing the radiation pressure gradient as a first order solution of radiative transfer equation: $dP_{\text{rad}}/d\tau = -(F_0/c) e^{-\tau}$, and integrating of hydrostatic balance from 0 to τ , we obtain:

$$P_{\text{gas}}(\tau) = P_{\text{gas}}(0) - \frac{1}{\kappa} \left(\frac{GM_{\text{BH}}}{r^2} - \Omega^2 r \right) \tau - \frac{F_0}{c} e^{-\tau} + \frac{F_0}{c} \quad (9)$$

where c means velocity of light.

At the illuminated face of the cloud, the total pressure has some constant initial value: $C_0 = P_{\text{gas}}(0) + F_0/c$. In addition the gas pressure gradient at the outer cloud surface ($\tau = \tau_{\text{max}}$) should be zero, since the cloud is finite and the radiation pressure and centrifugal force should balance the gravitational force there i.e. $(GM_{\text{BH}}/r^2 - \Omega^2 r)/\kappa = (F_0/c) e^{-\tau_{\text{max}}}$. Adopting those conditions the hydrostatic balance is:

$$P_{\text{gas}}(\tau) = C_0 - \frac{F_0}{c} (e^{-\tau} + \tau e^{-\tau_{\text{max}}}) \quad (10)$$

To put limits on the initial conditions of cloud pressure which fulfils the hydrostatic balance we express the ratio of gas pressure at two extreme cases: for $\tau = 0$ and $\tau = \tau_{\text{max}}$:

$$\frac{P_{\text{gas}}(\tau_{\text{max}})}{P_{\text{gas}}(0)} = \frac{C_0 - \frac{F_0}{c} e^{-\tau_{\text{max}}} (1 + \tau_{\text{max}})}{C_0 - \frac{F_0}{c}} \quad (11)$$

The above equation does not put any limit on the initial values of cloud pressure being in pressure equilibrium. We can consider special limits. Assuming $\tau_{\text{max}} \ll 1$, we get:

$$\frac{P_{\text{gas}}(\tau_{\text{max}})}{P_{\text{gas}}(0)} = 1; \Rightarrow P_{\text{gas}} = \text{const} \quad (12)$$

which is well known case of constant gas pressure cloud. It means that for optically thin clouds we don't have strong modification of the gas pressure by the radiation

pressure. Second special case occurs for $\tau_{\text{max}} \gg 1$, and we get:

$$\frac{P_{\text{gas}}(\tau_{\text{max}})}{P_{\text{gas}}(0)} = \frac{C_0}{C_0 - \frac{F_0}{c}} = 1 + \frac{P_{\text{rad}}(0)}{P_{\text{gas}}(0)} \quad (13)$$

In this case the density gradient inside the cloud depends on the adopted value of gas to radiation pressure at the illuminated face of cloud. When $P_{\text{rad}}(0) \ll P_{\text{gas}}(0)$ again we get condition of cloud being under constant gas pressure. But when $P_{\text{rad}}(0) \geq P_{\text{gas}}(0)$, the compression of cloud by radiation pressure is always present and increases with increasing value of this ratio. Thus the requirement that radiation pressure should be much larger from the gas pressure, made by [Baskin, Laor & Stern \(2014\)](#) for RPC model, is only the special case among solutions for constant pressure cloud, where the compression is the strongest. Physically, it is always the case of warm absorbers in AGN modelled by [Róžańska, Kowalska & Gonçalves \(2008\)](#). Nevertheless, many other solutions of clouds being under constant total pressure are possible from small compression equivalent to constant gas pressure model up to strong RPC considered by [Baskin, Laor & Stern \(2014\)](#) in case of BLR.

Physical conditions considered in this paper, needed to give strong emission at ILR, put us into the limit of $P_{\text{rad}}(0) < P_{\text{gas}}(0)$ by roughly two orders of magnitude depending on the cloud location. However, constant gas pressure even in this case is not equivalent to constant density model, since even constant gas pressure can imply large density and temperature gradient. To illustrate the difference between CP and CD clouds within the framework of our model we present in [Figs. 2](#) the structure of a single cloud as a result of photoionization calculations with CLOUDY code. Our cloud is located at 1 pc from SMBH and illuminated by SED of Mrk 509. The assumed density on the cloud surface is of the order of $n_{\text{H}} = 10^{10} \text{ cm}^{-3}$. The difference between assumption of constant density (dashed blue line) and constant pressure (solid red line) is noticeable. The density structure for CP cloud is not constant, even when compression is very weak, since radiation pressure is gradually absorbed with cloud optical depth.

Lower gas pressure at illuminated cloud surface can relatively increase the compression by radiation pressure. Physically we can achieve this condition for lower density. In [Fig. 3](#) we present the same single cloud comparison for density of the order of 10^5 cm^{-3} . For such case we are in the limit where $P_{\text{rad}}(0) \approx P_{\text{gas}}(0)$ and compression is clearly visible as a density and gas pressure rise up with cloud thickness. Nevertheless, recently we have shown that ILR can exist only if density is high ([Adhikari et al. 2016](#)), which means our CP clouds are not too strongly compressed, and therefore not so dif-

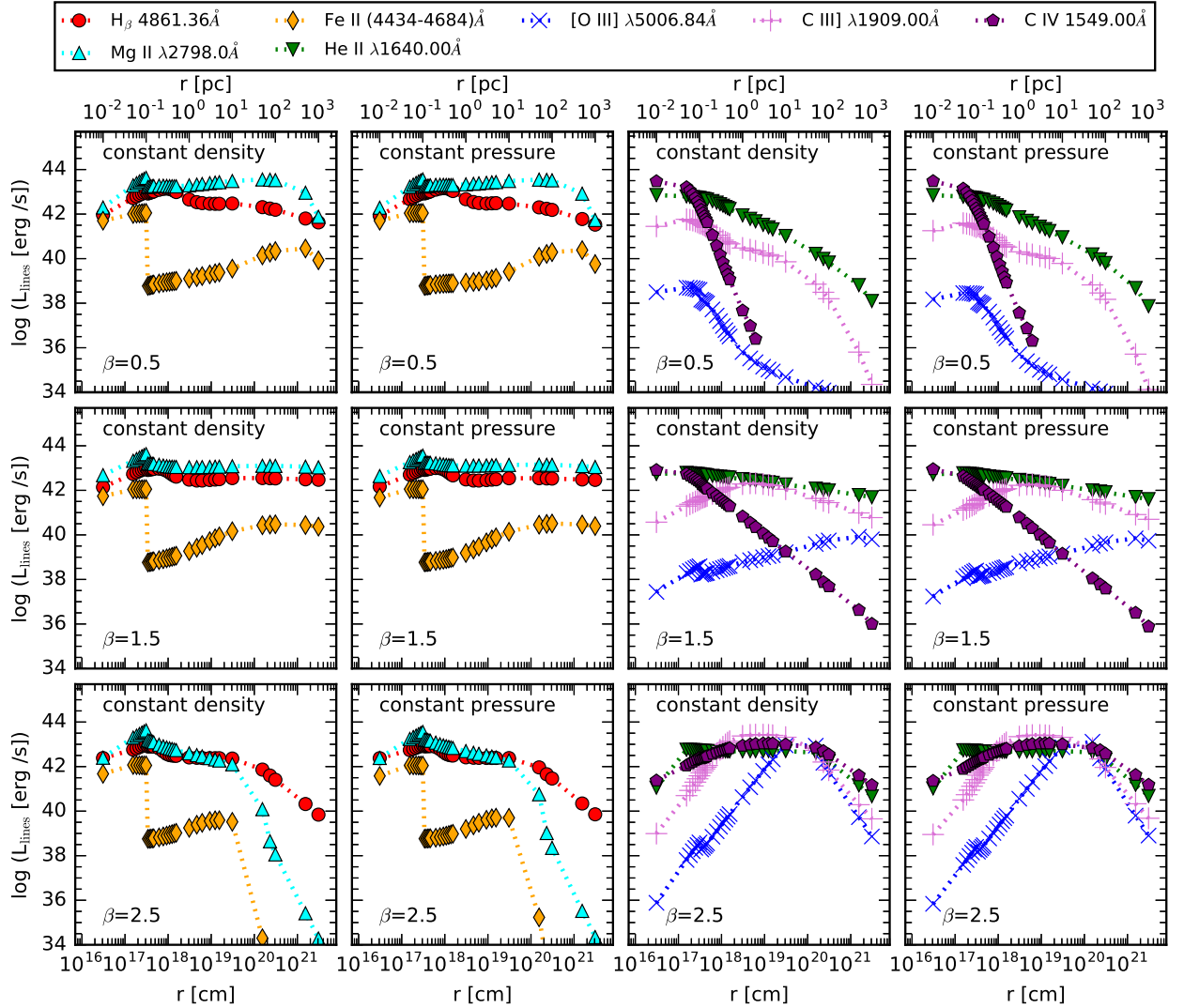


Figure 4. Line luminosity versus radius for Mrk 509, Sy 1.5 SED. Left two column panels represent LIL: H β Mg II and Fe II lines for constant density and constant pressure case respectively, while right two columns show HIL: He II, C III], [O III], and C IV lines again for constant density and constant pressure respectively. Three row panels show cases for $\beta = 0.5, 1.5$ and 2.5 from top to the bottom.

ferent from CD model.

The requirement of high density cloud at the sublimation radius sets the sound-crossing timescale to be two orders of magnitude smaller than the dynamical timescale, which is expected to be a few years at $R_d = 0.1$ pc. Cooling/heating timescale for such dense gas is even several orders of magnitude shorter than sound-crossing timescale, therefore we assume that clouds are both in thermal and hydrostatic equilibrium. With such assumption, even dense clouds can survive for at least a fraction of the local Keplerian period without being destroyed.

3.2. CP versus CD for full model

With above considerations, we derived the line luminosities for the major emission lines, which we present in Fig. 4 for the case of Sy1.5 galaxy Mrk 509 spectral

shape. For better visibility we draw emission from LIL: H β , Mg II, and Fe II in the left two panel columns, while other HIL as: He II, C III], [O III], and C IV are show in right two panel columns.

Each pair of panel columns in Fig. 4 represents the comparison between the model which assumes that each cloud is computed under constant density, to the model which assumes CP clouds. We can easily see that emission line luminosities do not differ when more physical model of CP is used. Profiles of all emission lines are practically the same, when we compare left and right column of both pairs of column panels. We demonstrate here that for such colder clouds as in BLR and NLR, the compression by radiation pressure is not that important as in warm absorbers studied by Rózańska et al. (2006); Adhikari et al. (2015). As shown in previous subsec-

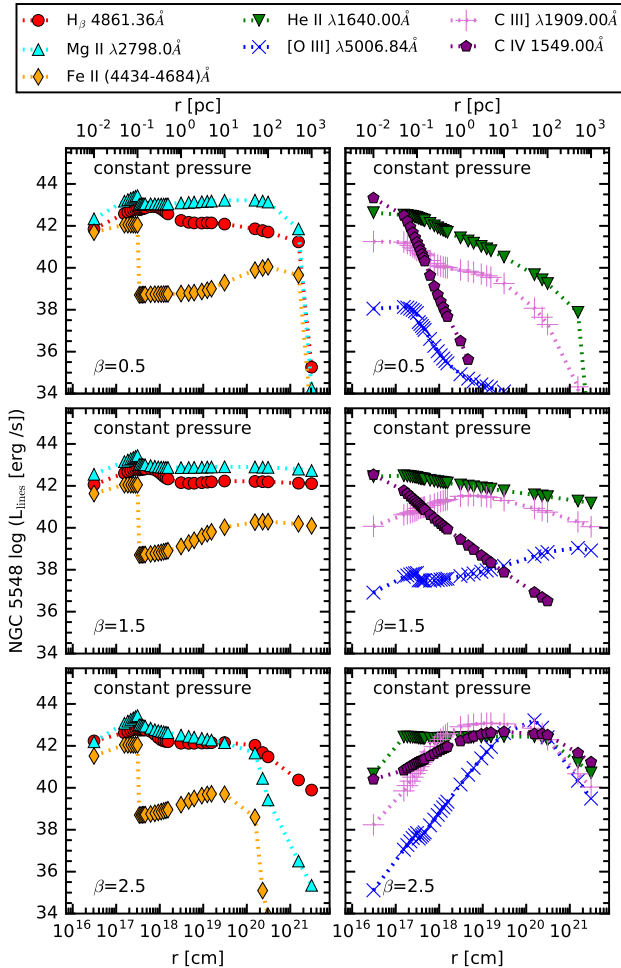


Figure 5. Line luminosity versus radius for NGC 5548, Sy 1 SED. Left column panel represents LIL: $H\beta$, Mg II and Fe II, while right column shows HIL: He II, C III], [O III], and C IV, for constant pressure model. Three row panels show cases for $\beta = 0.5, 1.5$ and 2.5 from top to the bottom.

tion, we may expect some differences for lower density normalization at a sublimation radius. But for lower density we are not able to produce visible ILR region, which is a purpose of this paper. The above conclusion is valid for all four spectral shapes used in this paper, therefore for other AGN types we present only CP models of line emissivity in Figs. 5, 6, and 7.

3.3. The density power-law slope

Only for $\beta = 1.5$, the overall line emissivity profiles stay flat along the radius in case of four AGN types, with exception of Fe II and C IV lines. The density profile with such power law slope changes from $\sim 10^{12} \text{ cm}^{-3}$ in BLR to $\sim 10^6 \text{ cm}^{-3}$ in NLR with the later value favorable by narrow lines.

The situation changes when $\beta = 0.5$, and density still is high $\sim 10^{9.5} \text{ cm}^{-3}$ in NLR. All LIL as $H\beta$, Mg II and Fe II, presented always on left column panels, display

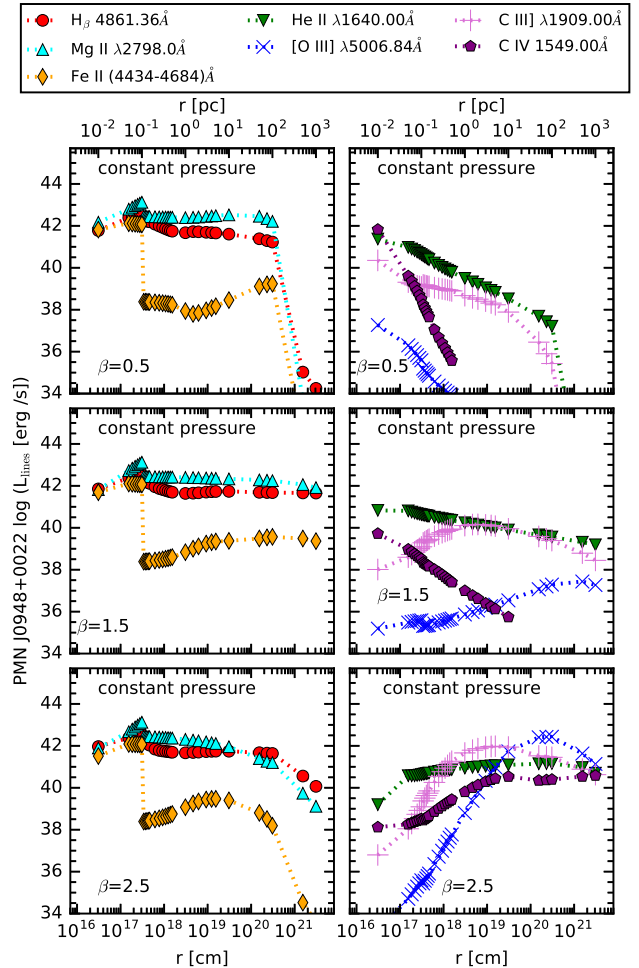


Figure 6. The same as in Fig. 5, but for PMN J0948+0022, NLSy1 SED

sudden drop in emissivity in the NLR range $r \gtrsim 100 \text{ pc}$, caused by the low value of ionization parameter (due to high density). The exception is Mrk 509 (Fig. 4, because there are many of UV photons in its spectral shape (Fig. 1 dashed-red line). The high value of those photons still keeps the ionization parameter high enough to produce strong LIL. On the other hand HIL, presented always on right column panels decrease monotonically with distance.

On the second extrema, when $\beta = 2.5$, the density is very low $\sim 10^{1.5} \text{ cm}^{-3}$ in NLR. This provides to the visible drop of LIL in the NLR range $r \gtrsim 100 \text{ pc}$, caused by too low density. It happens in all types of AGN. Nevertheless, the emission of HIL increases with the distance from SMBH up to the point about $r \sim 10 \text{ pc}$ due to relatively high ionization parameter. Further away from the center, such emission becomes flat or decreases depending on the value of ionization parameter.

In general results do not depend much on SED shape and in all cases ILR is visible with exception of Fe II

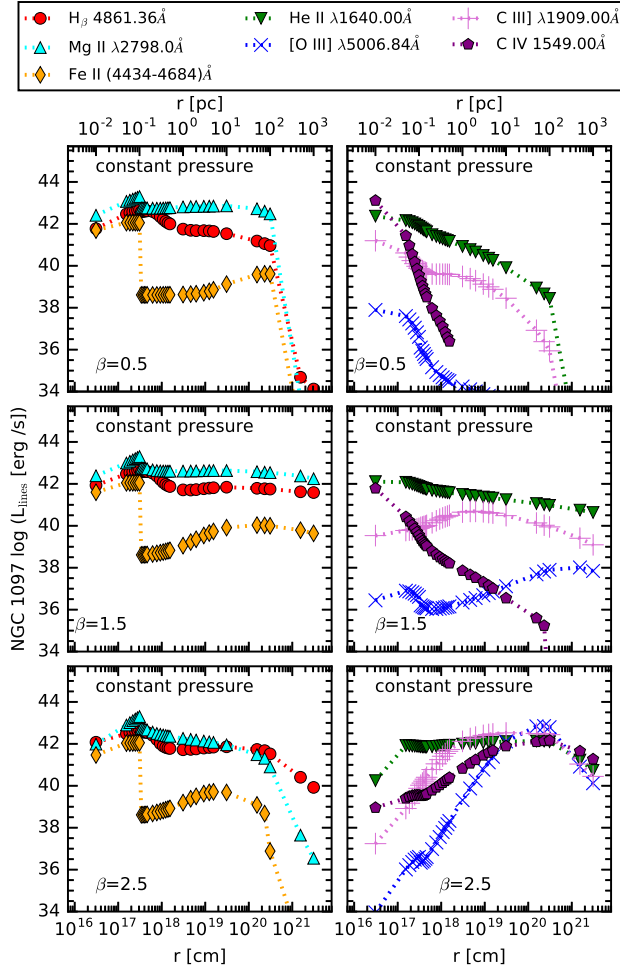


Figure 7. The same as in Fig. 5, but for NGC 1097, LINER SED.

permitted and [O III] forbidden lines. Forbidden lines are effectively produced in low density environment and for many cases presented here their emissivity is too low.

3.4. Dust sensitive Fe II line

In all cases, the Fe II line is the only line which shows strong emissivity drop by several orders of magnitude at the sublimation radius. Such behavior predicts the lack of intermediate component for this line. Therefore, based on the results of our simulations, the Fe II line is sensitive to the presence of dust, and it is not ILR indicator.

In our model, strong Fe II emissivity drop may be caused by two effects. The first one is the presence of dust discussed above, but the second effect can be the change of abundances in the gas phase when passing sublimation radius. The assumed solar composition for $r < R_d$ has two orders of magnitude higher iron abundance than ISM composition for $r > R_d$. All other elements display the same magnitude abundances when changing from solar to ISM composition. The change

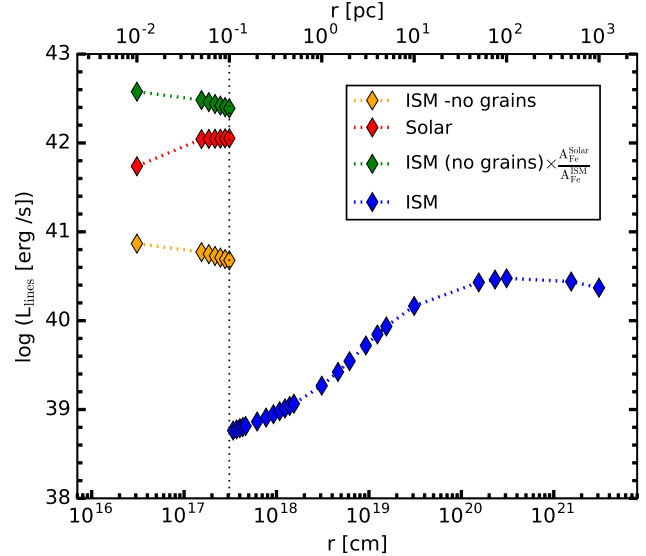


Figure 8. The comparison of Fe II line luminosity for two models of clouds illuminated by Mrk 509 SED with different abundances of dustless clouds. The ISM composition with grains is used for dusty clouds located further than R_d , marked by vertical dotted line. For clouds located closer to SMBH than R_d we plotted Fe II line luminosity for Solar iron abundance by red diamonds and for ISM without grains abundance by orange diamonds. Green diamonds mark the ISM model without grains multiplied by the Fe abundance ratio of those two models.

of abundances mimics the depletion of metals due to dust sublimation as it was already assumed by NL93 and AD16. In order to check what really causes the strong drop of Fe II emissivity profile at R_d , we made a test with different abundances in dustless clouds located at BLR. Results are presented in Fig. 8, where we compare two models. In the first model, we assume ISM chemical composition with no grains for BLR clouds, while in the second model, the same clouds have typical solar abundances. In both models ISM composition with grains is used for dusty clouds located further than R_d . It is clearly seen that the dust present is responsible for the Fe II emissivity drop by about two orders of magnitude, while the change in iron abundance enhances this effect by one order of magnitude.

4. DISK-LIKE DENSITY PROFILES

Since many years, it was postulated that at different radii we should have outflows from disk atmosphere in AGN (i.e. Elvis 2004). In this section we consider disk-like density profile, $n_H(r)$, which is expected where clouds are formed from outflowing gas above the accretion disk atmosphere. We do not specify the mechanism which provides to the formation of clouds, we only assume they do exist and they should have the same density as upper disk atmosphere. For determination of cloud disk-like density profile, we have to specify disk

parameters, as black hole mass and accretion rate for each type of AGN. Table 1 displays all important values used in our further computations.

By adopting black hole masses and accretion rates, we simulate the vertical accretion disk structure assuming standard [Shakura & Sunyaev \(1973\)](#) disk and transfer of radiation by diffusion approximation with gray gas opacities as described by [Róžańska et al. \(1999\)](#). Furthermore, we employ the cloud radial density profile by the requirement that the adopted gas density at the illuminated cloud surface equals to the disk atmosphere density where $\tau = 2/3$, i.e. the atmosphere is still optically thick. When this comparison is done at each distance from the black hole, we obtain disk-like cloud density profile.

The disk-like density profiles for all sources are presented at Fig. 9. The characteristic feature of such radial density profiles possess strong density rise up to 10^{15} cm^{-3} , located around the position of BLR, $r \sim 10^{-2}$ pc. This is caused by strong opacity hump in an accretion disk atmosphere. Outside density hump its values decline from about 10^{13} cm^{-3} at the distance of 10^{15} cm from black hole, to about a few 10^9 cm^{-3} at further distances of 10^{19} cm. The corresponding ionization parameters for each disk-like density profiles are presented in Fig. 10. One can see noticeable difference between ionization degree, which is four orders of magnitude lower for LINER than Sy1 and NLSy1 case. In addition, the density hump is directly reflected in the ionization drop in all sources.

In this section, the source luminosity, L , given in third column of Table 1 is obtained by the integration of flux between the energy range from 1 to 10^5 eV. Furthermore, the dust sublimation radius, R_d for each source luminosity is computed using the following formula given by [Nenkova et al. \(2008\)](#):

$$R_d = 0.4\sqrt{L/10^{45}} \quad [\text{pc}]. \quad (14)$$

This formula simply indicates the radius at which, for a given luminosity, the gas temperature reaches the value of 1400 K. Below this temperature dust can survive as a substantial gas component. The sublimation radius corresponding to each type of AGN is given in 6th column of Table 1. It is clear that the luminosity influences the position of sublimation radius, which we fully take into account in this section. In addition, the normalization of N_H to $10^{23.4}$ cm^{-2} differs for each source, since it is set at the position of sublimation radius.

The position of sublimation radius strongly depends on the detailed dust composition which is still under discussion ([Gaskell 2017](#); [Xie, Li & Hao 2017](#)). The dust is most likely the mixture of amorphous carbon ([Czerny et al. 2004](#)), silicate ([Lyu, Hao & Li 2014](#)) and graphite grains ([Baskin & Laor 2018](#)), while the sub-

Table 1. Parameters used in computations of disk-like density profile and the position of R_d . The first and second column lists the name of AGN and its type. The integrated luminosity is given in third column. The black hole masses in $10^7 M_\odot$, and accretion rates in units of Eddington accretion rate, follow in fourth and fifth column respectively. Both values are taken from literatures listed below. The derived dust sublimation radius in 10^{17} cm is given in column six.

| Name | AGN type | $L_{(1-10^5)\text{eV}}$ erg s^{-1} | M_7^{BH} M_\odot | \dot{m} \dot{M}_{Edd} | R_{17}^d cm |
|-----------|----------|--|--------------------------------|-------------------------------------|------------------|
| Mrk 509 | Sy1.5 | 6.62×10^{45} | 14^a | 0.30^b | 31.6 |
| NGC 5548 | Sy1 | 1.28×10^{44} | 6.54^c | 0.02^d | 4.41 |
| PMN J0948 | NLSy1 | 2.28×10^{46} | 15.4^e | 0.40^f | 58.9 |
| NGC 1097 | LINER | 9.62×10^{40} | 14^g | 0.0064^h | 0.12 |

a – [Mehdipour et al. \(2011\)](#), b – [Boissay et al. \(2014\)](#), c – [Bentz et al. \(2007\)](#), d – [Crenshaw et al. \(2009\)](#); [Ho & Kim \(2014\)](#), e – [Foschini et al. \(2011\)](#), f – [Abdo et al. \(2009\)](#), g – [Onishi et al. \(2015\)](#), h – [Nemmen, Storchi-Bergmann & Eracleous \(2014\)](#).

limation radius derived by [Nenkova et al. \(2008\)](#) corresponds to the temperature of sublimation of silicate grains only ([Laor & Draine 1993](#)). Graphite grains sublimate at larger temperature up to ~ 2000 K ([Laor & Draine 1993](#); [Baskin & Laor 2018](#)), nevertheless AGN extinction curves do not show the 2175\AA carbon feature ([Maiolino et al. 2001](#)) which makes the dust in the circumnuclear region of AGNs being different from Galactic ISM. Nevertheless, to show how our results do depend on the dust sublimation radius, below we present our model computed for two sources with sublimation radius about 10 times lower: $R_d = 0.06\sqrt{L/10^{45}}$ pc, which corresponds to graphite sublimation temperature ([Laor & Draine 1993](#)).

We assume that emitting clouds directly emerge from the disk’s atmosphere and preserve its density along the whole range of radii. This is reasonable assumption at least for low ionization part of the BLR as it may develop as a failed wind embedded in the disk’s atmosphere ([Czerny & Hryniewicz 2011](#)). On the other hand, this assumption is the same as the model of BLR being a part of accretion disk atmosphere ([Baskin & Laor 2018](#)). Our approach is not in contradiction with line emitting medium geometry similar to bowl on top of the accretion disk ([Gaskell 2009](#); [Goad, Korista & Ruff 2012](#)).

Resulting line emissivity profiles for four sources, are presented in Fig. 11 – HIL and LIL, and Fig. 12 – only LIL. In addition, for each source we present total dust and total gas emission by magenta solid and black dashed lines respectively. Shaded areas on the figures mark the position of BLR, ILR and NLR which depends on the AGN type. Assuming that all emitting gas is dominated by Keplerian motion, BLR marked with pink shadow spans between 15000 km s^{-1} down to 3000 km s^{-1} . ILR marked with green shadow spans be-

tween 3000 km s^{-1} and 900 km s^{-1} , while NLR marked with violet shadow spans between 900 km s^{-1} down to 300 km s^{-1} .

In all AGN types, the emissivity profiles of LIL are insensitive to the density hump in disk-like cloud density profile. On the other hand, HIL display strong luminosity drop which reflects the density enhancement in the cloud radial profile. Such HIL luminosity drop is usually situated in BLR indicating the division of BLR on two types of low and high ionization as previously suggested by Collin-Souffrin et al. (1988); Collin et al. (2006); Czerny & Hryniewicz (2011).

In case of PMN J0948 and Mrk 509, luminosity is high enough to push sublimation radius above 0.1 pc making part of the ILR free from dust. This allows for appearance of emissivity maximum within ILR below sublimation radius (three upper panels of Fig. 11). Thus, in Seyferts, our model predicts dominating intermediate component in LIL: $\text{H}\beta$, Mg II , and Fe II . Their line luminosities rise monotonically up to sublimation radius. Nevertheless, the emission of HIL: He II , C III , $[\text{O III}]$, and C IV is maximal in outer BLR or inner ILR, and decreases with distance.

In case of LINER, dust sublimation radius appears at the position of HIL emissivity drop, caused by cloud density hump, because of its low luminosity. The presence of dust in BLR region provides to flat line emissivities all the way to NLR. Therefore, ILR could be present in LINER, but it is not as strong as in other types of AGN. Our result confirms the statement made by Balmaverde et al. (2016), where the authors concluded that high density component of inner portion of ILR is visible in Seyferts whereas the entirety of ILR emission is visible in LINER. Nevertheless, the density of ILR clouds in LINER inferred by those authors is 10^{4-6} cm^{-3} , less by ~ 5 orders of magnitude than the density of the ILR clouds in our model. We predict for NGC 1097, the location of ILR at the range of radii $0.07-0.8 \text{ pc}$ whereas, the distance of ILR inferred by Balmaverde et al. (2016) is $1-10 \text{ pc}$.

In general, for disk-like density profile, additional lines as Mg II and slightly $\text{H}\beta$, appear to be dust sensitive. Their luminosity profiles exhibit rapid decrease when dust appears in clouds located relatively far from the center. This does not happen in case of LINER, since dusty clouds are still very dense (Fig. 12 fourth panel).

The disk-like density cloud distribution model is less general, than arbitrarily taken density profile in locally optimal clouds model Goad & Korista (2014), but it heavily depends on the conditions in disk's upper atmosphere. The results are also different. While in our model emissivity of $\text{H}\beta$ line increases with distance by two orders of magnitude for Seyfert AGN, Goad & Korista (2014) has shown decline of this line

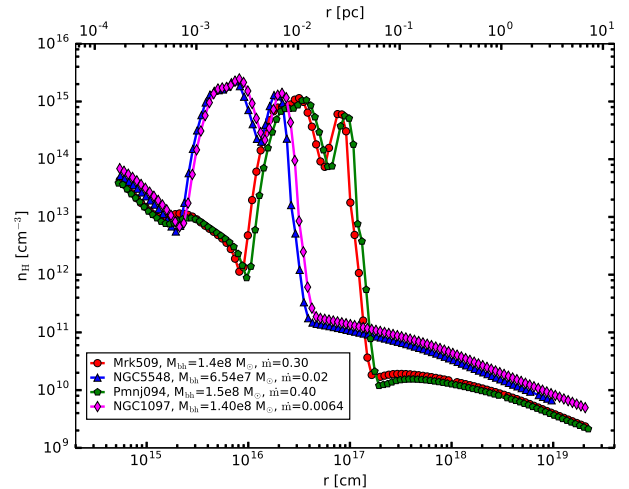


Figure 9. Radial density profiles as expected from the upper zones of accretion disk atmospheres for all considered sources: Parameters used in computations of the corresponding density profiles are also shown in the legend box.

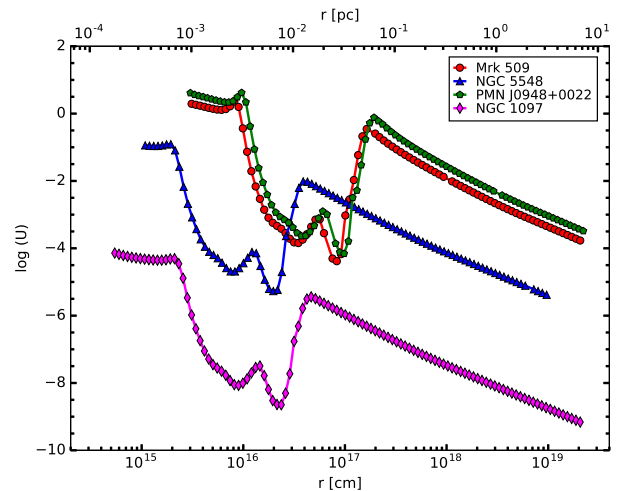


Figure 10. Radial ionization parameter U profiles at the cloud surface computed by Eq. 2 for disk-like density profiles as shown in Fig. 9.

between 1 and 100 light days. The consequence would be that our model predicts stronger importance of ILR component.

5. EMISSION LINE REGIONS

Syfert 1 – NGC 5548 is one of the best studied AGN. It has been regularly monitored for almost four decades. Thus it is clear that model of this source could be discussed most critically. We can compare approximate distances of emitting regions from our model with the results of reverberation mapping campaigns. We are aware of, that reverberation mapping depends on the continuum luminosity measurement (Peterson et al. 2004; Bentz et al. 2006, 2007; Denney et al. 2009), and

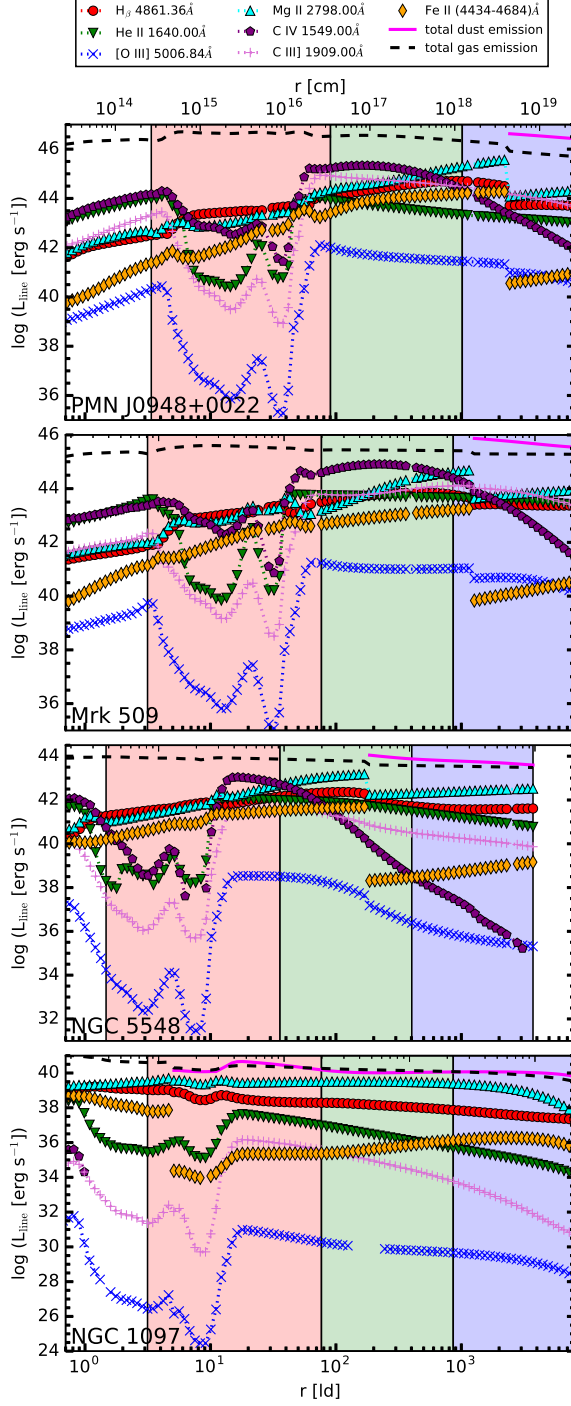


Figure 11. LIL and HIL luminosities versus radius (in light days) obtained for disk-like cloud density profiles. Each panel shows one type of AGN in the way that the source luminosity (given in Table 1) decreases from the top to the bottom panel. Shaded areas mark the position of BLR, ILR and NLR from the left to right respectively, based on the adopted range of Keplerian velocities (see text for details).

data show delays measurements in $H\beta$ span over 6-30 days depending on the continuum luminosity. Therefore, in case of $H\beta$ line, we made analysis for continuum luminosity, $L_\lambda(5100\text{\AA})$, derived from incident SED

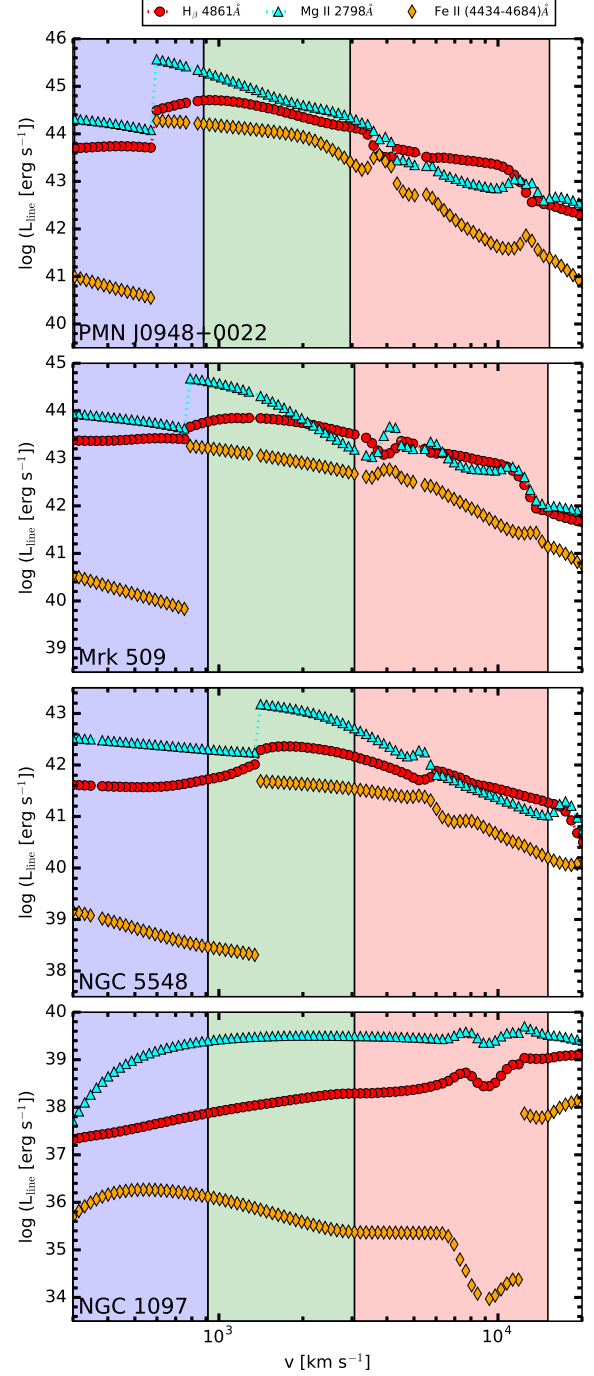


Figure 12. LIL luminosities versus Keplerian velocity obtained for disk-like cloud density profiles. Each panel shows one type of AGN in the way that the source luminosity (given in Table 1) decreases from the top to the bottom panel. Shaded areas mark the position of BLR, ILR and NLR from the right to left respectively, based on the adopted range of Keplerian velocities (see text for details).

(Fig. 1), and have checked what radius of the $H\beta$ emission we should expect from observational measurements (Kilerci Eser et al. 2015). For $\log L_\lambda(5100\text{\AA}) \approx 43.25$ used in our model, we have delay in $H\beta$ of the order of

20 days and line width $\text{FWHM} \approx 4700 \text{ km s}^{-1}$. Similar results were obtained by [Peterson et al. \(1991\)](#) using ground-based observations made in 1989, where 21 days delay between continuum and $\text{H}\beta$ was reported. Those observed parameters correspond to the radius at which the $\text{H}\beta$ line luminosity reaches maximum at about $4 \times 10^{17} \text{ cm}$ in our model (Fig. 11 third panel).

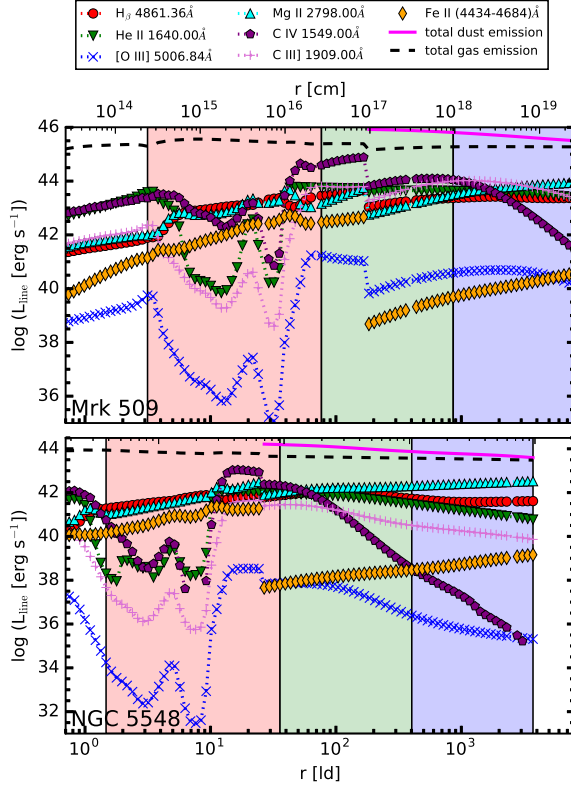


Figure 13. The same as in Fig. 11 for two best observed sources, Mrk 509 (upper panel) and MGC 5548 (lower panel), but for sublimation radius computed from the formula: $R_d = 0.06\sqrt{L/10^{45}}$ ([Laor & Draine 1993](#)).

However recent observations of velocity resolved reverberation mapping presented by [Pei et al. \(2017\)](#) show new points which do not agree with the fitted trend of $L_\lambda(5100\text{\AA})$ versus $\text{H}\beta$ delay ([Kilerci Eser et al. 2015](#)). Those new points for $\log L_\lambda(5100\text{\AA}) \gtrsim 43.3$ present $\text{H}\beta$ delay of the order of 3 days, so shorter than even for the lowest, $\log L_\lambda(5100\text{\AA}) \approx 42.5$, luminosity state. [Lu et al. \(2016\)](#) derived BLR response delay to the source luminosity change to be 2.4 years. During this time, BLR may be rebuilt under change of radiation pressure, thus making the comparison of our model to the data more difficult.

NGC 5548 emissivity profile of both low ionization lines $\text{H}\beta$ and Mg II is very similar in our model (Fig. 12 third panel). However it is not exactly the case in reverberation mapping observations. Mg II line is more puz-

zling in this case. [Clavel et al. \(1991\)](#) presented peak-center delays from multimonth IUE campaign done in 1989. They have found very broad response in Mg II line covering 34–72 days. In addition, [Cackett et al. \(2015\)](#), analyzing Mg II variability have found only weakly correlated broad response to the continuum brightening, with delay response spanning 20–70 days range. Both results may suggest that line luminosity global maximum is located in ILR, which fully agrees with our model. However, even shallower, global line luminosity maximum in $\text{H}\beta$ located at the same region of our model is not resolved in the observations of delay. Mg II shows more luminous ILR with maximum before face of the torus. Brighter ILR in magnesium line should be reflected in higher average delays than in hydrogen Balmer lines and this is the case in reverberation measurements.

For the case of NGC 5548, [Clavel et al. \(1991\)](#) presented light-curves of C III] and C IV for which the delay covers approximately 26–32 days and 8–16 days respectively. This is consistent with the position of global maximum in the emissivities of those lines further on and at the outer edge of dense BLR, which fully agrees with our model. This is also explained by [Negrete et al. \(2013\)](#), who inferred emission radius of those high ionization lines from the photoionization condition. They found optimal emission of C IV for $n_H = 10^{12} \text{ cm}^{-3}$, $\log U \approx -2$ and C III], and for $n_H = 10^{10} \text{ cm}^{-3}$, $\log U \approx -1.5$ which is consistent with our model as seen in Fig. 10. C III] emissivity in ILR is rather flat and allows noticeable emission originating from clouds located at higher radii.

The permitted He II line is always broad and blended with semi-forbidden O III], therefore the measurements of delay covering 4–10 days are more difficult to explain by our model. Such delay corresponds to the location of emissivity drop of He II line in the dense BLR in NGC 5548 (see third panel of Fig. 11). Our model predicts that the He II luminosity local maximum is located on the outer edge of the dense BLR for expected ≈ 20 days delay.

HST monitoring described by [De Rosa et al. \(2015\)](#) reveal C IV delay of 5 days and He II delay of 2.5 days. This again corresponds to the emissivity drop of our model. Those results may demand stronger modification of our model. For instance, gaseous clouds presented on higher elevation above the disk where density departure from the atmospheric value may be significant. Such geometry for broad high ionization line regions were already postulated in the literatures (i.e. [Collin et al. 2006](#); [Decarli et al. 2008](#); [Kollatschny & Zetzl 2013](#)).

To check how the position of dusty torus (discussed in Sec. 4) influences radial emissivity profile, in Fig. 13 we present the case of two best studied sources computed for 10 times smaller value of sublimation radius

taken as $R_d = 0.06\sqrt{L/10^{45}}$ (Laor & Draine 1993). For Mrk 509, Koshida et al. (2014) have reported 120-150 days delay of dust phase, depending on the method of derivation. This value fully agrees with the position of sublimation radius from the formula by Laor & Draine (1993), presented in upper panel of Fig. 13. However, this fact would eliminate dominance of 1000 km/s component in Mg II line and possibly would remove intermediate width line component of global emissivity maximum of $H\beta$. This brings our model closer to the observed line delays. In case of NGC 5548, Koshida et al. (2014) derived inner torus face radius comparing optical and near infrared variability. Their measurements cover range from 60 to 80 days depending on the NGC 5548 continuum luminosity and method used in calculations. This is over 3 times larger than sublimation radius by Laor & Draine (1993) (lower panel of Fig. 13, and 2 times smaller than the one computed by Eq. 14. The lower position of sublimation radius in NGC 5548 influences maximum emissivity of Mg II shifting it to the lower radii and decrease contribution from 2000 km/s component.

Peterson et al. (2013) investigated variability of forbidden [O III] line in NGC 5548. They found delay between 10-20 years ($\sim 2-3$ pc) and suggested emitting medium with density 10^5 cm^{-3} . While NLR studied in X-rays, as suggested by Detmers, Kaastra & McHardy (2009), covers 1-15 pc or more precisely 14 pc as derived by Whewell et al. (2015). In our model densities corresponding to NLR remain high ($\approx 10^9 \text{ cm}^{-3}$). We have high emissivities of narrow components in all permitted lines except C IV. In addition, [O III] emissivity remains rather low. Crenshaw, Boggess & Wu (1993) reported strong narrow components in all optical/UV permitted lines, especially C IV. Thus our model is less accurate reproducing NLR, for assumed disk-like density profile.

Mrk 509 model is in many aspect similar to the NGC 5548. The most noticeable difference is shift in the emissivity maximum of C III] and C IV toward greater radii. This predicts stronger intermediate emission line components from our model. And this seems to be the case when we look at the observational spectra, presented for example by Negrete et al. (2013). Our model computed for NLSy1-PMN J0948 shows very similar emissivity profile shapes to those of Mrk 509 as those sources have similar BH masses but different SEDs. However, line luminosity to the continuum luminosity ratio is lower for NLSy1, thus effectively broad components blend with continuum and only contrast of narrow components remain sufficient to make line visible. The LINER case of NGC 1097 is exceptional because the sublimation radius is inside our dense BLR. This fact makes all line luminosity profiles flat up to NLR, which is in agreement with Balmaverde et al. (2016) who empha-

sized the extended ILR in LINERS up to 10 pc. In case of flat radial luminosity profile, narrow component has the highest contrast, therefore it will dominate line profile, which is in agreement with González-Martín et al. (2015), who pointed out that AGN dominated LINERS are very similar to Seyfert 2 galaxies.

6. CONCLUSIONS

We carried out the photoionization simulations of the ionized gas clouds in AGNs and studied the effect of varying density profiles on the line emission across the radial distance that spans all the way from BLR down to the NLR. The different density prescriptions are applied in the following ways: a) we employed the density profile as simple power law used by NL93 and AD16, and varied its slope. b) We self consistently computed the disk-like density profiles for each AGN by using their observed properties; black hole mass and Eddington ratio.

Using the various density profiles derived, we computed the line luminosities of the major emission lines in Sy1.5 Mrk 509, Sy1 NGC 5548, NLSy1 PMN J0948+0022 and LINER NGC 1097 differing by their SEDs. Below we list final conclusions:

1. In case of clouds located at distances considered in this paper, CP and CD cloud models reproduce exactly the same line luminosity profiles in the regime of lines observed in optical/UV. It is caused by the fact that our clouds are dense. Lower density clouds do not produce the ILR.
2. The varying slope of the power law density profile does not affect the nature of the ILR. In particular, the intermediate emission in $H\beta$ is present for all the slopes independent of the SED shape.
3. For the lower slope of the density profile, forbidden [O III] and semi-forbidden C III] lines are strongly suppressed because of the high density environment. As the slope becomes more steeper, i.e. density decreases, these lines are prominent at radial distances corresponding to NLR.
4. Fe II emission line appeared to be most sensitive on the dust presence, since its luminosity drops by two orders of magnitude at the sublimation radius (see Sec. 3 for details).
5. The density drop in the disk-like density profiles causes mild enhancement of Mg II, $H\beta$ and Fe II lines, while He II, C III] and [O III] are suppressed at the density drop location. This result is consistent with separation of LIL and HIL clouds in two-component BLR model (Collin-Souffrin et al. 1988).

6. The low luminosity of the LINER NGC 1097 shifts the dust sublimation radius toward smaller distances from SMBH, which makes the emissivity profiles of all lines flat. Therefore, intermediate line component can be detectable, but is less prominent than the narrow line component.
7. The distance inferred from the time delay of $H\beta$, Mg II, in NGC 5548 taken from reverberation mapping closely agrees with the distance at which the $H\beta$ line peaks in the simulated line emissivity profile.
8. The NLR from our disk-like model is denser as it is postulated from observations. NLR clouds may become rare while escaping from accretion disk atmosphere, which we plan to take into account in

the future paper.

This research was supported by Polish National Science Center grants No. 2015/17/B/ST9/03422, 2015/18/M/ST9/00541, 2015/17/B/ST9/03436, 2016/21/N/ST9/03311 and by Ministry of Science and Higher Education grant W30/7.PR/2013. It received funding from the European Union Seventh Framework Program (FP7/2007-2013) under the grant agreement No.312789. TPA received funding from NCAC PAS grant for young researchers. GJF thanks the Nicolaus Copernicus Astronomical Center for its hospitality and acknowledges support by NSF (1108928, 1109061, and 1412155), NASA (10-ATP10-0053, 10-ADAP10-0073, NNX12AH73G, and ATP13-0153), and STScI (HST-AR-13245, GO-12560, HST-GO-12309, GO-13310.002-A, HST-AR-13914, and HST-AR-14286.001).

Software: CLOUDY (v17.00; (Ferland et al. 2017))

REFERENCES

- Abdo A. A. et al., 2009, ApJ, 699, 976
 Adhikari T. P., Róžańska A., Czerny B., Hryniewicz K., Ferland G. J., 2016, ApJ, 831, 68
 Adhikari T. P., Róžańska A., Hryniewicz K., Czerny B., Ferland G. J., 2017, Frontiers in Astronomy and Space Sciences, 4, 19
 Adhikari T. P., Róžańska A., Sobolewska M., Czerny B., 2015, ApJ, 815, 83
 Balmaverde B., Capetti A., Moisió D., Baldi R. D., Marconi A., 2016, A&A, 586, A48
 Baskin A., Laor A., 2018, MNRAS, 474, 1970
 Baskin A., Laor A., Stern J., 2014, MNRAS, 438, 604
 Bentz M. C. et al., 2007, ApJ, 662, 205
 Bentz M. C., Peterson B. M., Pogge R. W., Vestergaard M., Onken C. A., 2006, ApJ, 644, 133
 Boissay R. et al., 2014, A&A, 567, A44
 Boroson T. A., Green R. F., 1992, ApJS, 80, 109
 Brotherton M. S., Wills B. J., Francis P. J., Steidel C. C., 1994, ApJ, 430, 495
 Cackett E. M., Gültekin K., Bentz M. C., Fausnaugh M. M., Peterson B. M., Troyer J., Vestergaard M., 2015, ApJ, 810, 86
 Clavel J. et al., 1991, ApJ, 366, 64
 Collin S., Kawaguchi T., Peterson B. M., Vestergaard M., 2006, A&A, 456, 75
 Collin-Souffrin S., Dyson J. E., McDowell J. C., Perry J. J., 1988, MNRAS, 232, 539
 Crenshaw D. M., Boggess A., Wu C.-C., 1993, ApJ, 416, L67
 Crenshaw D. M., Kraemer S. B., 2007, ApJ, 659, 250
 Crenshaw D. M., Kraemer S. B., Schmitt H. R., Kaastra J. S., Arav N., Gabel J. R., Korista K. T., 2009, ApJ, 698, 281
 Czerny B., Hryniewicz K., 2011, A&A, 525, L8
 Czerny B., Li J., Loska Z., Szczerba R., 2004, MNRAS, 348, L54
 Czerny B. et al., 2017, ArXiv e-prints
 —, 2015, Advances in Space Research, 55, 1806
 D’Ammando F. et al., 2015, MNRAS, 446, 2456
 Davidson K., 1972, ApJ, 171, 213
 De Rosa G. et al., 2015, ApJ, 806, 128
 Decarli R., Labita M., Treves A., Falomo R., 2008, MNRAS, 387, 1237
 Denney K. D. et al., 2009, ApJ, 704, L80
 Detmers R. G., Kaastra J. S., McHardy I. M., 2009, A&A, 504, 409
 Dopita M. A., Groves B. A., Sutherland R. S., Binette L., Cecil G., 2002, ApJ, 572, 753
 Dumont A.-M., Abrassart A., Collin S., 2000, A&A, 357, 823
 Elvis M., 2004, in Astronomical Society of the Pacific Conference Series, Vol. 311, AGN Physics with the Sloan Digital Sky Survey, Richards G. T., Hall P. B., eds., p. 109
 Ferland G. J. et al., 2017, ArXiv e-prints
 Foschini L. et al., 2011, MNRAS, 413, 1671
 Gaskell C. M., 2009, New A Rev., 53, 140
 —, 2017, MNRAS, 467, 226
 Goad M. R., Korista K. T., 2014, MNRAS, 444, 43
 Goad M. R., Korista K. T., Ruff A. J., 2012, MNRAS, 426, 3086
 González-Martín O. et al., 2015, A&A, 578, A74
 Grevesse N., Sauval A. J., 1998, Space Sci. Rev., 85, 161
 Ho L. C., Kim M., 2014, ApJ, 789, 17
 Hu C., Wang J.-M., Ho L. C., Chen Y.-M., Bian W.-H., Xue S.-J., 2008a, ApJ, 683, L115
 Hu C., Wang J.-M., Ho L. C., Chen Y.-M., Zhang H.-T., Bian W.-H., Xue S.-J., 2008b, ApJ, 687, 78
 Kaastra J. S. et al., 2011, A&A, 534, A36
 Kilerci Eser E., Vestergaard M., Peterson B. M., Denney K. D., Bentz M. C., 2015, ApJ, 801, 8
 Kollatschny W., Zetzl M., 2013, A&A, 551, L6
 Koshida S. et al., 2014, ApJ, 788, 159
 Krolik J. H., McKee C. F., Tarter C. B., 1981, ApJ, 249, 422
 Laor A., Draine B. T., 1993, ApJ, 402, 441
 Lu K.-X. et al., 2016, ApJ, 827, 118
 Lyu J., Hao L., Li A., 2014, ApJ, 792, L9
 Maiolino R., Marconi A., Salvati M., Risaliti G., Severgnini P., Oliva E., La Franca F., Vanzì L., 2001, A&A, 365, 28
 Mason K. O., Puchnarewicz E. M., Jones L. R., 1996, MNRAS, 283, L26
 Mehdipour M. et al., 2011, A&A, 534, A39
 —, 2015, A&A, 575, A22
 Negrete C. A., Dultzin D., Marziani P., Sulentic J. W., 2013, ApJ, 771, 31

- Nemmen R. S., Storchi-Bergmann T., Eracleous M., 2014, MNRAS, 438, 2804
- Nenkova M., Sirocky M. M., Ivezić Ž., Elitzur M., 2008, ApJ, 685, 147
- Netzer H., 1990, in *Active Galactic Nuclei*, Blandford R. D., Netzer H., Woltjer L., Courvoisier T. J.-L., Mayor M., eds., pp. 57–160
- Netzer H., Laor A., 1993, ApJ, 404, L51
- Onishi K., Iguchi S., Sheth K., Kohno K., 2015, ApJ, 806, 39
- Osterbrock D. E., Ferland G. J., 2006, *Astrophysics of gaseous nebulae and active galactic nuclei*
- Pei L. et al., 2017, ApJ, 837, 131
- Peterson B. M. et al., 1991, ApJ, 368, 119
- , 2013, ApJ, 779, 109
- , 2004, ApJ, 613, 682
- Róžańska A., Czerny B., Życki P. T., Pojmański G., 1999, MNRAS, 305, 481
- Róžańska A., Goosmann R., Dumont A.-M., Czerny B., 2006, A&A, 452, 1
- Róžańska A., Kowalska I., Gonçalves A. C., 2008, A&A, 487, 895
- Shakura N. I., Sunyaev R. A., 1973, A&A, 24, 337
- Whewell M. et al., 2015, A&A, 581, A79
- Xie Y., Li A., Hao L., 2017, ApJS, 228, 6
- Zhu L., Zhang S. N., Tang S., 2009, ApJ, 700, 1173